UDK 631.824:620.193:57.012.3
Original scientific article/Izvirni znanstveni članek

ISSN 1580-2949
MTAEC9, 58(5)577(2024)

# COMPARISON OF CORROSION BEHAVIORS OF B1, BA11, BZ11 AND BC11 MAGNESIUM ALLOYS

## PRIMERJAVA KOROZIJSKIH LASTNOSTI MED MAGNEZIJIVIMI ZLITINAMI TIPA B1, BA11, BZ11 IN BC11

**Zhiwen Mao, Zheng Jia*, Sichao Du, Yongzhi Yu**

College of Mechanical Engineering, Shenyang University, Shenyang 110044, China

*Prejem rokopisa – received: 2024-05-25; sprejem za objavo – accepted for publication: 2024-08-21*

doi:10.17222/mit.2024.1205

The Mg-Bi alloy, commonly referred to as the "green metal," finds extensive applications in industries such as automotive and aerospace due to its exceptional corrosion resistance. The corrosion performance of this alloy is intricately linked with its elemental composition. In this investigation, four distinct types of homogeneous magnesium alloys were meticulously prepared: Mg-1Bi (B1), Mg-1Bi-1Al (BA11), Mg-1Bi-1Al (BZ11), and Mg-1Bi-1Cu (BC11). Subsequently, a comprehensive analysis was conducted to examine the microstructures and corrosion behaviors exhibited by these magnesium alloys, exposed to a 3.5 *w*/% NaCl aqueous solution. The corrosion resistance test reveals that the corrosion resistance ranking of the four materials is as follows: BZ11 > BA11 > B1 > BC11. Among them, the uniform state of BZ11 alloy exhibits the lowest corrosion rate, measuring 0.548 mm·y$^{-1}$, primarily attributed to its fine grain size and a small amount of dispersed second phase particles. Conversely, the uniform state of BC11 alloy demonstrates inferior corrosion resistance due to a high content of second phase particles within the alloy composition. SEM and EDS techniques were employed for microstructure characterization of all four magnesium alloys. The results indicate that localized corrosion occurs in all four alloys, with the electrochemical corrosion between the second phase particles and the matrix being specifically identified as the primary cause for degradation of BC11 alloy. XRD analysis confirms that in Mg-Bi alloy, the $\alpha$-Mg phase coexists with block- or strip-shaped $Mg_3Bi_2$ phases as secondary phases. In contrast, BA11 and BZ11 alloys exhibit no change in secondary phases, consisting mainly of the $\alpha$-Mg phase and $Mg_3Bi_2$ phase. On the other hand, BC11 alloy predominantly contains the $\alpha$-Mg phase, $Mg_3Bi_2$ phase, and reticular $Mg_2Cu$ as secondary phases.

Keywords: Mg-Bi alloy, indirect extrusion, alloying, corrosion properties, corrosion products

Zlitine tipa Mg-Bi se pogosto omenjajo kot "zelene" zlitine in se danes močno uveljavljajo za uporabo v industriji, kot na primer v avtomobilski in letalski industriji, zaradi njihove dobre odpornosti proti koroziji. Korozijske lastnosti te vrste zlitin so močno odvisne od njihove kemijske sestave in vsebnosti glavnih legirnih elementov. V tem članku avtorji opisujejo raziskavo štirih točno določenih tipov natančno izdelanih homogenih Mg zlitin. Izbrali so zlitine tipa Mg-1Bi (B1), Mg-1Bi-1Al (BA11), Mg-1Bi-1Zn (BZ11) in Mg-1Bi-1Cu (BC11). Po izdelavi zlitin so izvedli ustrezno mikrostrukturno in korozijsko preiskavo zlitin s potapljanjem njihovih preizkušancev v vodno raztopino s 3,5 *w*/% NaCl. Na osnovi korozijskih preiskav so avtorji ugotovili naslednji vrstni red odpornosti proti koroziji vseh štirih zlitin: BZ11 > BA11 > B1 > BC11. Med vsemi je najbolj enovito stanje izražala zlitina BZ11, pri kateri so ugotovili majmanjšo hitrost korozije (0,548 mm·leto$^{-1}$), ki jo pripisujejo njeni mikrostrukturi z majhno velikostjo kristalnih zrn in majhno vsebnostjo delcev sekundarne faze. Nasprotno pa je zlitina BC11 imela najslabšo odpornost proti koroziji zaradi visoke vsebnosti delecev sekundarne faze. Rezultati mikrostrukturnih preiskav in mikrokemijskih analiz pod vrstičnim elektronskim mikroskopom (SEM/EDS) so pokazali, da je pri vseh štirih zlitinah prišlo do lokalne elektro-kemijske korozije med delci sekundarnih faz in kovinsko matrico, kar je bil še posebej primarni vzrok za degradacijo zlitine BC11. XRD analize so nadalje potrdile, da v Mg-Bi zlitinah medsebojno obstajata (koeksistirata) $\alpha$-Mg faza in faza $Mg_3Bi_2$ v obliki blokov ali trakov sekundarne faze. Pri zlitinah BA11 in BZ11 ni prišlo do spremembe tipa sekundarne faze $Mg_3Bi_2$ v $\alpha$-Mg matrici. Po drugi strani pa je v zlitini BC11 prevladovala $\alpha$-Mg matrica ter v njej disperzija sekundarnih faz $Mg_3Bi_2$ in mrežaste $Mg_2Cu$.

Ključne besede: Mg-Bi zlitine, indirektna ekstruzija, alloying, korozijske lastnosti, korozijski produkti

## 1 INTRODUCTION

Magnesium (Mg) is the lightest structural metal. Compared with steel, aluminum alloys, and engineering plastics, magnesium alloys have excellent properties such as being lightweight, having high specific strength, high thermal conductivity, and resistance to electromagnetic interference.[1,2] However, magnesium corrodes in most inorganic acidic and neutral solutions, which still restricts a widespread application of magnesium alloys. Typically, alloying can improve the performance of magnesium alloys by changing the grain size and altering the chemical composition, distribution, and volume fraction of precipitated phases. Mg-Bi alloy is a common type of magnesium alloy, and the bismuth content can affect the corrosion resistance of magnesium alloys. Bismuth (Bi) is non-toxic and known as a "green metal". Adding bismuth to an Mg-Al alloy can refine $Mg_{17}Al_{12}$ and form a needle-like $Mg_3Bi_2$ phase.[3] Xu et al. investigated the influence of 0.2 *w*/% and 0.8 *w*/% bismuth on the corrosion resistance of Mg-xBi ($x$ = 0.2 *w*/% and 0.8 *w*/%) binary alloys, suggesting that when the bismuth content reaches 0.8 % (*w*/%), a composite oxide film composed of an insoluble $Bi_2O_3$ compound deposited on the surface

*Corresponding author's e-mail:
jz140@163.com (Zheng Jia)

of the matrix, along with porous $Mg(OH)_2$ forms, inhibits the penetration of corrosive media, thus improving the corrosion resistance of the alloy.[4] An addition of elements can change the chemical composition and microstructure of a material, thereby improving its corrosion resistance. Aluminum (Al) is commonly alloyed with magnesium to provide higher ductility, weldability, and corrosion resistance.[5] O. Lunder et al. studied the corrosion resistance of an AZ91 alloy in a 5-% NaCl solution and found that alloying magnesium with aluminum can enhance the activity of magnesium in electrochemical reactions, and aluminum added within a certain concentration range can act as a passivating agent.[6] After aluminum, zinc (Zn) is the second most commonly used alloying element in the magnesium alloy production. Yi et al. studied the effect of different zinc contents (0, 1, 2, 3) % on the corrosion resistance of Mg-Mn alloys.[7] They found that the alloy had optimal corrosion resistance with a zinc content of 1 %. However, as the zinc content continued to increase, the corrosion resistance of the alloy decreased. Additionally, it was shown that increasing the zinc content can lead to higher stress-corrosion-cracking susceptibility.[8] Zhang et al. investigated the corrosion behavior of an Mg-1Bi-1Zn-1Ag alloy in a SBF solution and observed filamentous and intergranular corrosion as its main forms.[9] The formation of these types of corrosion was attributed to a competition between the protective effects from product films and galvanic corrosion. Moreover, Yan et al. found that copper (Cu) exhibits excellent antibacterial properties, which could provide valuable insights for the future development of biological magnesium alloys.[10]

However, until now, there have been few studies on the effect of low contents of different alloying elements on the corrosion behavior of an Mg-Bi alloy in a 3.5 *w*/% NaCl solution. In this work, the corrosion processes of homogeneous (12 h, 400 °C) BA11, BZ11, BC11 and B1 alloys were studied using a hydrogen evolution weight loss test, electrochemical technology, polarizing detection methods, XRD, SEM and EDS characterization methods in order to reveal the influence of different alloying elements on the corrosion resistance of Mg-Bi alloys. The purpose of this study is to test this corrosion behavior, hoping that the addition of low contents of different elements can improve the corrosion performance of the alloy, and lay the foundation for subsequent research.

## 2 EXPERIMENTAL WORK

### *2.1 Material preparation*

The raw materials used to prepare ingots included pure Mg (99.99 *w*/%), pure Bi (99.99 *w*/%), pure Al (99.99 *w*/%), pure Zn (99.99 *w*/%) and pure Cu (99.99 *w*/%). The entire smelting process was conducted under a mixed protective atmosphere of $CO_2$ and $SF_6$ with a volume ratio of 100:1, respectively. The chemical compositions of the alloys were analyzed using inductively coupled plasma atomic emission spectroscopy (ICP-AES) and presented in **Table 1**. Subsequently, in order to improve the segregation of the as-cast structure and make the metal elements fully diffuse, the as-cast magnesium alloy was homogenized with heat treatment. Four alloy ingots were homogenized at 400 °C for 12 h and then quenched in water at room temperature. The four alloy ingots underwent a 12-hour homogenization process at 400 °C, followed by quenching with water at ambient temperature.

**Table 1:** Chemical compositions (*w*/%) of the studied alloys

| Alloy | Composition, *w*/% | | | | |
|---|---|---|---|---|---|
| | Mg | Bi | Al | Zn | Cu |
| Mg-1Bi | Bal. | 1.03 | – | – | – |
| Mg-1Bi-1Al | Bal. | 1.11 | 0.86 | – | – |
| Mg-1Bi-1Zn | Bal. | 1.05 | – | 0.94 | – |
| Mg-1Bi-1Cu | Bal. | 1.10 | – | – | 0.83 |

### *2.2 Microstructure characterization*

A Shimadzu-7000 XRD diffractometer was used to analyze samples polished to a particle size of 5000, in order to determine the composition of the second phase in the alloy. The alloy's microstructure was observed using an OLYMPUS SC50 metallographic microscope and an S4800 scanning electron microscope.

### *2.3 Corrosion analysis*

The corrosion behavior of sheets was studied using hydrogen evolution and electrochemical tests, which were repeated three times. All samples were mounted using epoxy resin, ground with 1500-5000 grit SiC papers, and polished so that the testing plane was parallel to the ED-transverse direction (TD). An exposed area of 10×10 $mm^2$ was considered, and a 3.5 *w*/% NaCl solution was used as the corrosive medium. After being immersed for 24 h, the morphology of corrosion products and removal products was examined using scanning electron microscopy (with the surface corrosion products eliminated through a chromic acid solution (200 $gL^{-1}$ $CrO_3$ + 10 $gL^{-1}$ $AgNO_3$) for 600 s, followed by ultrasonic wave agitation).

The hydrogen evolution experiment was conducted in a 3.5 *w*/% saturated NaCl solution at a temperature of 25 °C for a duration of 24 hours. An alloy sample was positioned within an inverted funnel, above which an dropper containing a 3.5 *w*/% NaCl solution was placed to collect the precipitated hydrogen gas, as shown in **Figure 1**. The corroded specimen was weighed to determine its mass loss. The corrosion rate of the alloy was calculated using formulas (1) and (2) to assess its corrosion resistance.

The weight loss corrosion rate:[11]

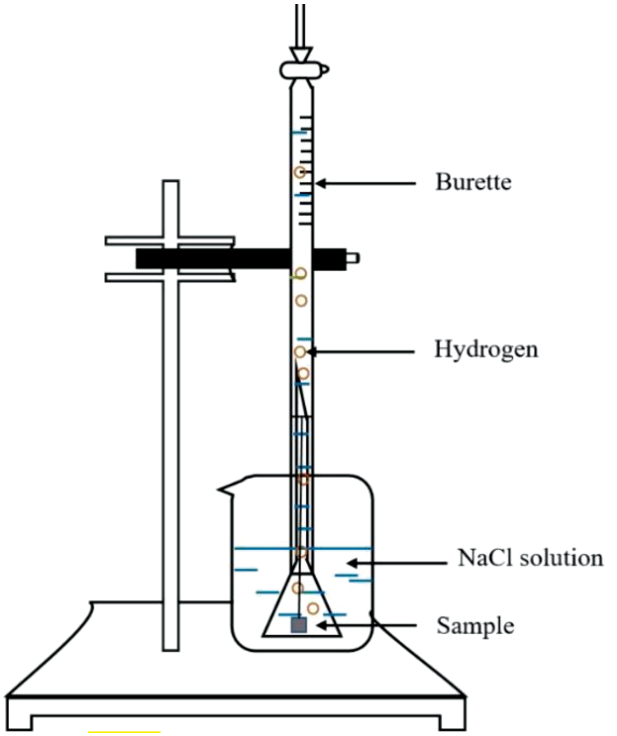


**Figure 1:** Hydrogen analysis experimental apparatus

$$P_w = \frac{8.76\times10^4\,\Delta g}{At\rho} \quad (1)$$

$P_W$: corrosion rate (mm·a$^{-1}$); $\Delta g$: reduced quality of the alloy before and after soaking (g); A: surface area of the sample (cm$^2$); t: corrosion time (h); $\rho$: density of the sample (g·cm$^{-3}$)

The hydrogen evolution corrosion rate:[12]

$$P_H = \frac{8.76\times10^4\,\Delta VM}{At\rho} \quad (2)$$

$P_H$: hydrogen evolution corrosion rate (mm·a$^{-1}$); $\Delta V$: total hydrogen (mL); $M$: relationship between the alloy mass loss rate and hydrogen precipitation rate, 0.001083 (g·mL$^{-1}$); $A$: sample surface area (cm$^2$); $t$: corrosion time (h); $\rho$: sample density (g·cm$^{-3}$)

For the electrochemical test, a three-electrode model (CHI660E) was utilized with a saturated calomel electrode serving as the reference electrode, a platinum electrode as the counter electrode and a magnesium alloy sample being tested as the working electrode. The open circuit potential (OCP) of the materials was measured for 3600 s. Electrochemical impedance spectroscopy (EIS) was conducted within a scanning frequency range of $10^{-6}$ Hz to $10^{-2}$ Hz. The data was fitted using Zsimpwin software through an equivalent circuit. The corrosion current density ($I_{corr}$) was estimated using the Tafel extrapolation method in the cathodic branch. The instantaneous corrosion rate $P_i$ (mm·a$^{-1}$) was correlated with $I_{corr}$ (mA·cm$^{-2}$). The instantaneous corrosion rate ($P_i$, mm·y$^{-1}$) was calculated as follows:[13,14]

$$P_i = I_{corr} \times 22.85 \quad (3)$$

## 3 RESULTS

### *3.1 Microstructure analysis*

The XRD patterns of the four homogeneous alloys are presented in **Figure 2**. In B1, BA11, and BZ11 alloys, only $\alpha$-Mg phase and $Mg_3Bi_2$ phase were observed. In BC11, in addition to the peaks corresponding to $\alpha$-Mg phase and $Mg_3Bi_2$ phase, a new peak corresponding to $Mg_2Cu$ phase was also discovered. The intensity of the peaks for $\alpha$-Mg phase and $Mg_3Bi_2$ phase in B1 alloy was low. An addition of 1 *w*/% Zn did not cause the formation of intermetallic compounds with Mg or Bi. The peak strength values of $Mg_3Bi_2$ phase in BA11 and BC11 alloys increased relative to those of B1 and BZ11 alloys.

**Figure 3** illustrates the polarization structure and distribution of grain sizes in the homogeneous alloys. The B1 alloy exhibits coarse grains, while additions of Al, Zn, and Cu refine it. The average grain size is shown in **Table 3**. Incorporating a single weight percent of Al reduces the grain size by 31 %, while Zn and Cu reduce it by 61 % and 43 %, respectively, in comparison with the homogeneous alloy without any additions. Notably, the refining effect achieved with 1 *w*/% Zn is comparable to that obtained with Cu as evidenced by the grain size distribution diagram.

SEM images of the alloys at low and high magnifications are presented in **Figure 4**. EDS results for the white areas are summarized in **Table 2**. In B1, BA11, and BZ11 alloys, a few rod and polyhedral eutectic structures are observed. The EDS results indicate that the Mg-to-Bi atomic ratio in the alloys is approximately 3:2, suggesting the presence of the $Mg_3Bi_2$ phase. Xu's research also produced similar results.[15] On the other hand, BC11 alloy exhibits a significant number of second phases precipitated along the grain boundaries, forming a network structure when connected with each other. The analysis

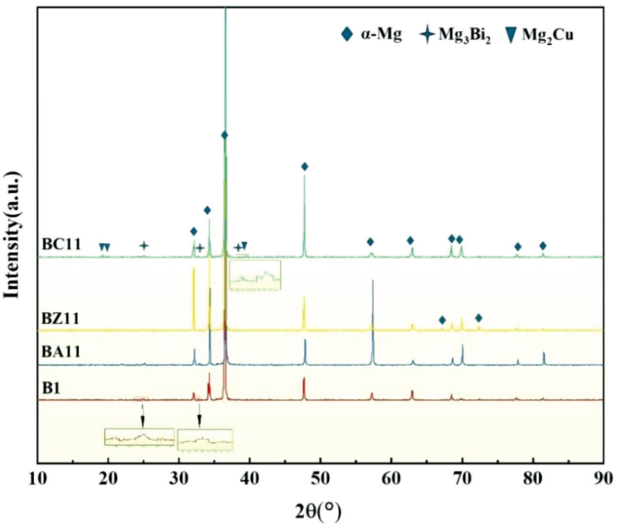


**Figure 2:** XRD patterns of homogenized alloys

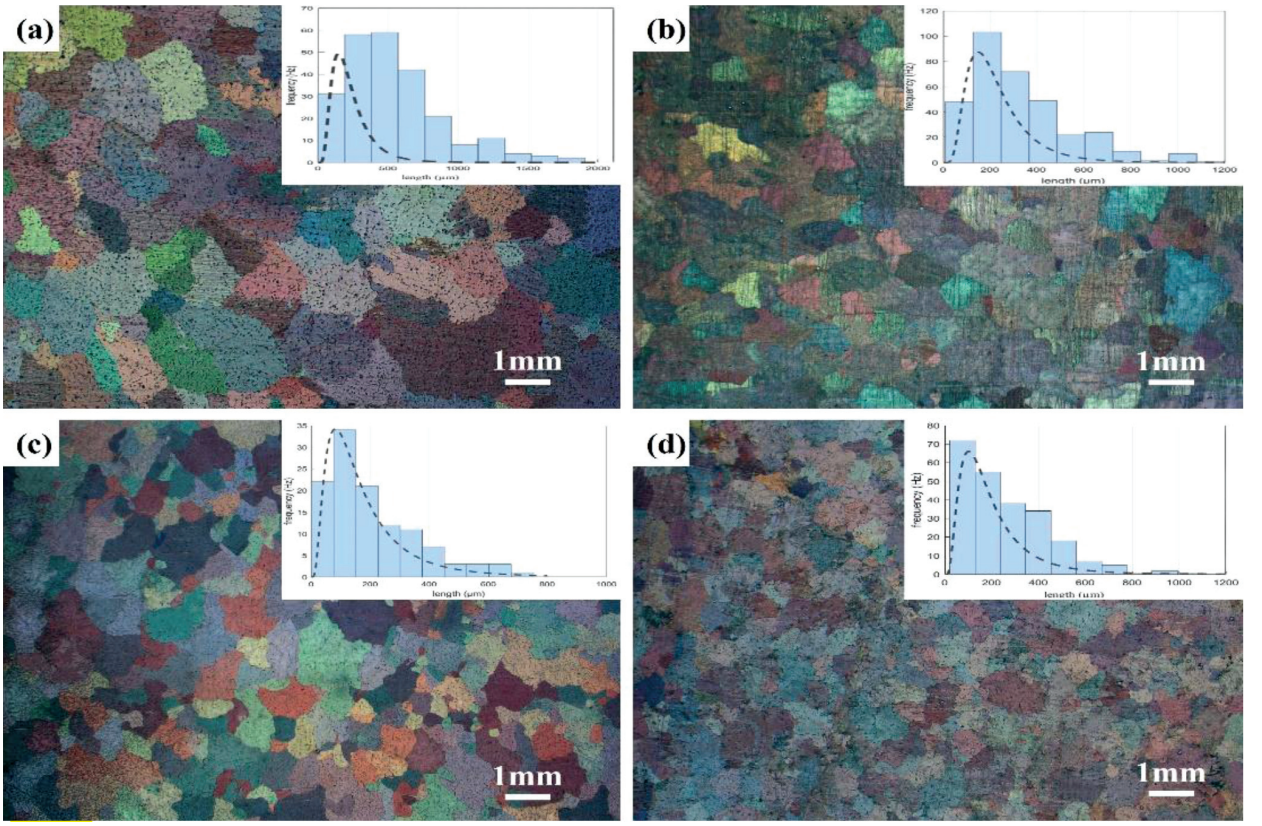


**Figure 3:** Polarized microstructure of the homogenized alloys and grain size distribution: a) B1, b) BA11, c) BZ11, d) BC11

from **Table 2** suggests that the alloys primarily consist of $Mg_2Cu$ and $Mg_3Bi_2$ phases during the second phase.

**Table 2:** EDS analysis of homogeneous alloys

| Alloy | Location | Particles | Element | | | | |
|---|---|---|---|---|---|---|---|
| | | | Mg | Bi | Al | Zn | Cu |
| B1 | A | $Mg_3Bi_2$ | 65.62 | 34.38 | – | – | – |
| | B | $Mg_3Bi_2$ | 90.38 | 9.62 | – | – | – |
| BA11 | C | $Mg_3Bi_2$ | 82.59 | 17.41 | – | – | – |
| | D | $Mg_3Bi_2$ | 67.68 | 32.14 | – | – | – |
| BZ11 | E | $Mg_3Bi_2$ | 77.04 | 22.96 | – | – | – |
| | F | $Mg_3Bi_2$ | 65.13 | 34.87 | – | – | – |
| BC11 | G | $Mg_2Cu$ | 82.71 | 0.94 | – | – | 16.34 |
| | H | $Mg_3Bi_2$ | 76.93 | 14.95 | – | – | 1.11 |
| | I | $Mg_2Cu$ | 77.06 | - | – | – | 22.94 |

**Table 3** shows the area fractions of the second phase of the alloys measured with Image pro software. Moreover, the average sizes of the second phases are measured with Matlab software. The area fraction and size of the second phase in B1 alloy are small, showing bar and point shapes. The addition of 1 *w*/% Al increased the average second-phase size and area fraction of the alloys. The addition of 1 *w*/% Zn hardly changes the area fraction of the second phase, nor does it change the size of the second phase, but the distribution of the second phase becomes more uniform than that of the B1 alloy (**Figure 4**). Introducing 1 *w*/% Cu enhances both the av-

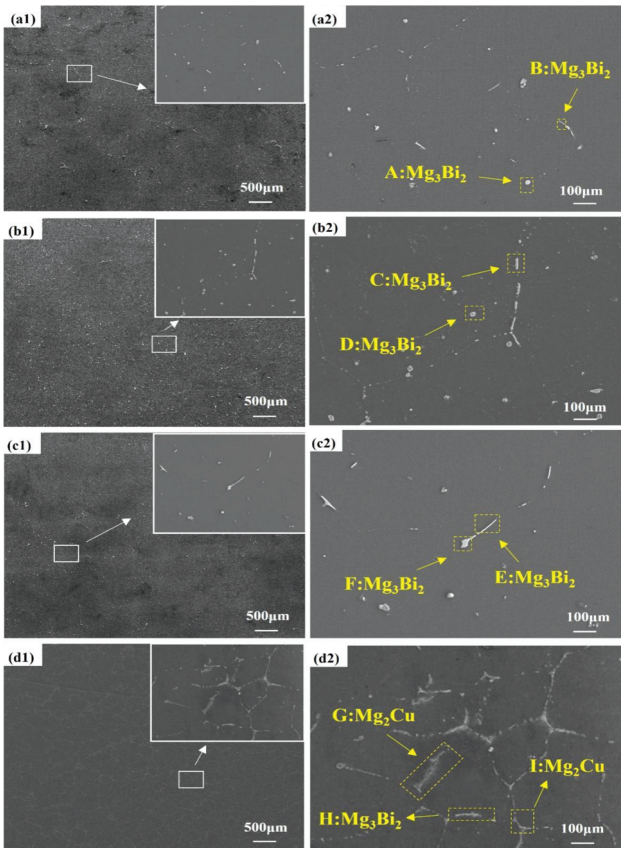


**Figure 4:** Scanning electron microscopy

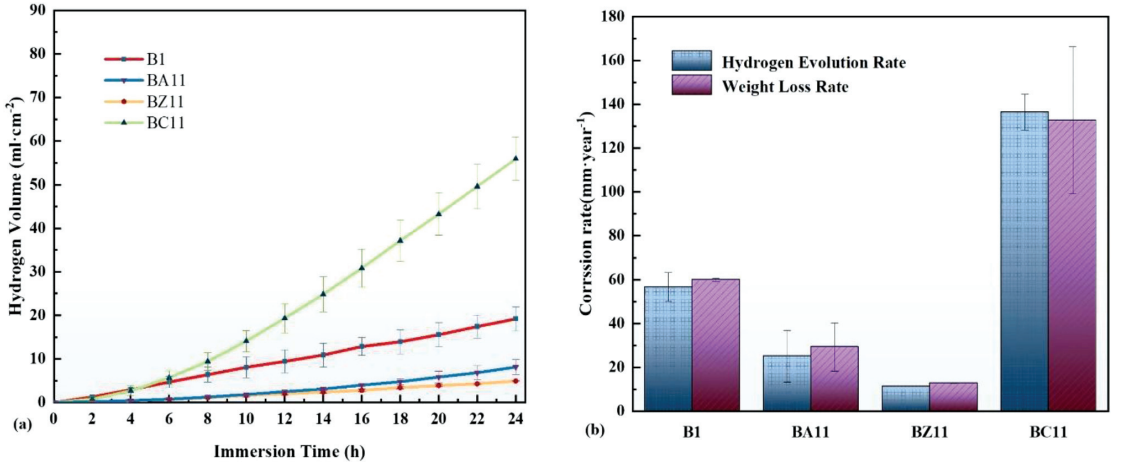


**Figure 5:** a) Amounts of hydrogen precipitation in homogeneous alloys after 24 h, b) hydrogen evolution loss corrosion rates of homogeneous alloys

erage size and area fraction of the precipitated phases. When combined with **Figure 2** findings, it can be concluded that the precipitation of $Mg_2Cu$ phase progressively enlarges both the area fraction and average grain size of the second phase along grain boundaries. **Table 3** shows the average second-phase size and area fraction of the homogeneous alloys.

**Table 3:** Mean dimensions and volumetric fraction of the secondary phase of homogeneous alloys

| Alloy | Average size (μm) | Area fraction |
|---|---|---|
| B1 | 5.73 | 0.10 ± 0.08 |
| BA11 | 6.36 | 0.26 ± 0.06 |
| BZ11 | 6.96 | 0.12 ± 0.06 |
| BC11 | 10.14 | 0.34 ± 0.05 |

### *3.2 Hydrogen evolution tests*

**Figure 5a** shows the hydrogen evolution volumes of the studied alloys after immersion in a 3.5 *w*/% NaCl solution for 24 h. It can be observed on **Figure 5a** that the BA11 and BZ11 alloys exhibit lower hydrogen precipitation amounts compared to the B1 alloy, while all three alloys (B1, BA11, and BZ11) demonstrate a nearly linear relationship between the hydrogen precipitation amount and corrosion time. It is postulated that the oxide film formed during the corrosion process either exhibits inadequate protective properties or fails to develop a protective coating on the surface. The hydrogen precipitation of BC11 alloy exhibits lower levels compared to B1 alloy within the first 4 hours, but experiences a rapid increase thereafter, surpassing that of B1 alloy significantly. This observation indicates poor corrosion resistance of BC11 alloy. **Figure 5b** illustrates the corrosion rates of the alloys in the descending order: BC11 > B1 > BA11 > BZ11. The hydrogen evolution weight loss rates for B1, BA11, BZ11, and BC11 alloys were measured at 56.59 mm·year$^{-1}$, 59.93 mm·year$^{-1}$, 25.06 mm·year$^{-1}$, and 29.28 mm·year$^{-1}$, respectively, while their corresponding hydrogen absorption weight gain rates were recorded at 11.34 mm·year$^{-1}$, 12.59 mm·year$^{-1}$, 136.41 mm·year$^{-1}$, and 132.67 mm year$^{-1}$.

### *3.3 Electrochemical analysis*

**Figure 6b** shows polarization curves of the studied samples after soaking in 3.5 *w*/% NaCl solution, and the electrochemical corrosion related parameters ($E_{corr}$, $I_{corr}$, $P_i$ and $R_p$) obtained from the polarization curves are summarized in **Table 4**, where $\beta\alpha$ and $\beta c$ represent the slopes of anode and cathode branches, respectively. The polarization resistance $R_p$ was calculated according to the corrosion parameters of the specimens.[16] The Ecorr value reflects the thermodynamic stability of the alloy and differs little from the Ecorr values of the four homogeneous alloys, indicating that their corrosion tendencies are similar.[17] Due to the negative difference effect (NDE) in the anode branch of magnesium alloy, the Tafel extrapolation method was used to calculate Icorr using the cathode branch.[18] The corrosion current density from high to low is BC11> B1> BA11 > BZ11. The higher the corrosion

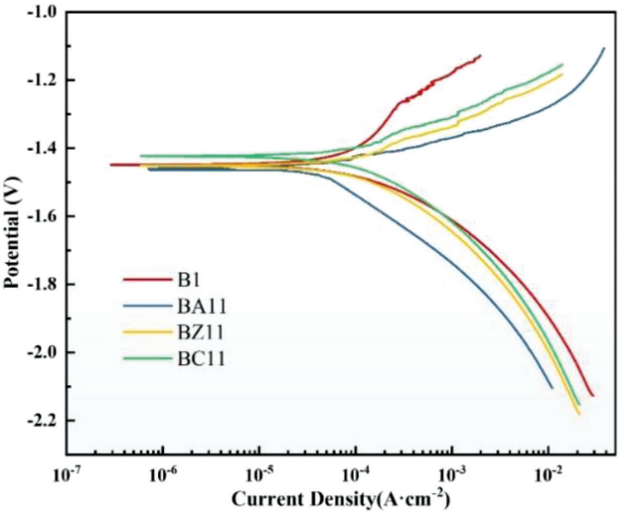


**Figure 6:** Polarization curves

**Table 4:** Electrochemical corrosion-related parameters

| | Polarization curve-related parameters | | | | | |
|---|---|---|---|---|---|---|
| | $I_{corr}$ (mA·cm$^{-2}$) | $E_{corr}$ (V) | Corrosion rate $P_i$ (mm·y$^{-1}$) | $\beta_a$ (V/dacade) | $\beta_c$ (V/dacade) | $R_p$ (Ω·cm$^2$) |
| B1 | 0.064 | –1.45V | 1.462 | 0.207 | –0.120 | 515.38 |
| BA11 | 0.038 | –1.46V | 0.868 | 0.065 | –0.185 | 549.62 |
| BZ11 | 0.024 | –1.52V | 0.548 | 0.070 | –0.154 | 870.65 |
| BC11 | 0.066 | –1.42V | 1.508 | 0.092 | –0.139 | 364.19 |

current density, the smaller are the charge transfer resistance and the corrosion resistance of the material.[19] After adding 1 *w*/% Al and 1 *w*/% Zn, $R_p$ increases from 515 Ω to 549 Ω and 870 Ω, respectively, while after adding 1 *w*/% Cu, $R_p$ decreases from 515 Ω to 364.19 Ω. Therefore, the corrosion resistance, shown in the order from large to small, is BZ11, BA11, B1, BC11.

In order to provide a more comprehensive analysis of the corrosion process observed in the studied samples, **Figure 7** presents Bode diagrams, Nyquist diagrams, phase angle plots and equivalent circuit diagrams. Additionally, **Table 5** summarizes the calculated values wherein $R_s$ represents the solution resistance, $CPE_{dl}$ denotes the capacitance between a sample and electrolyte solution, while $R_{ct}$ signifies the charge transfer resistance. Notably, $CPE_{dl}$ and $R_{ct}$ are employed in parallel to represent capacitive circuits at high frequencies. The resistance of the corrosion product film and the capacitance of the oxide film are represented as $R_f$ and $CPE_f$, respectively, in order to describe capacitor circuits oper-

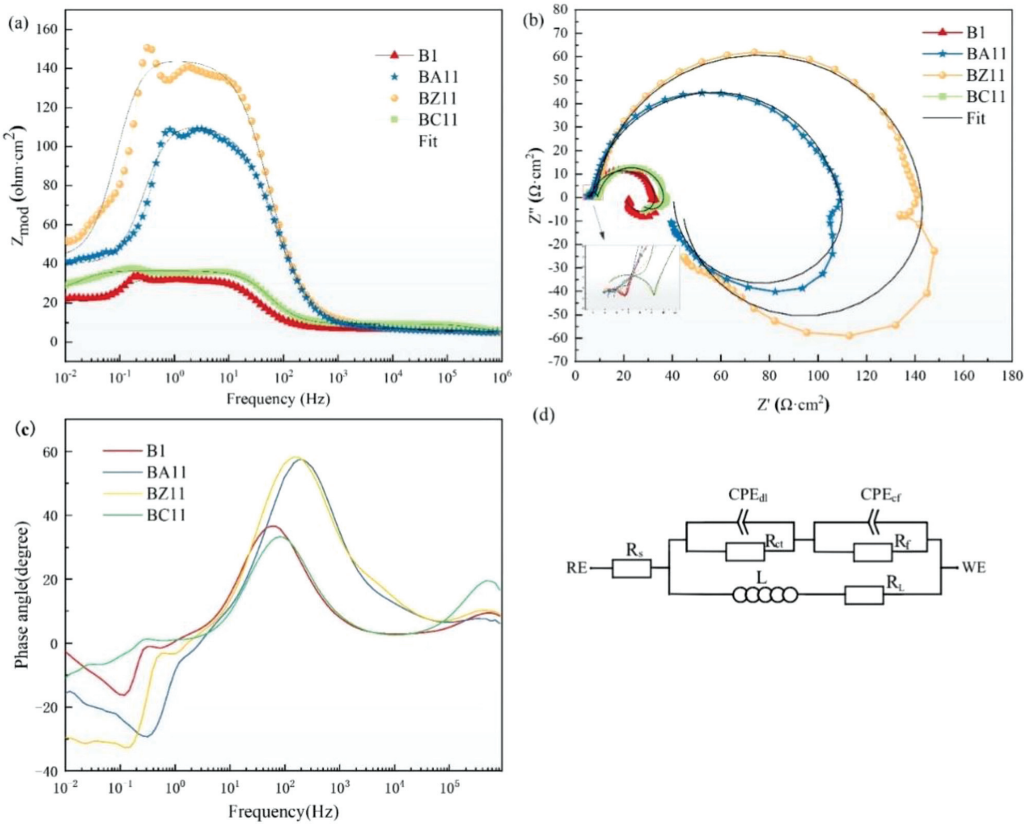


**Figure 7:** Electrochemical impedance spectrum (EIS) plots of the as-homogenized alloys: a) Bode diagrams, b) Nyquist curves, c) phase angle plots, d) circuit diagrams

**Table 5:** Fitting results for electrochemical impedance spectra of the as-homogenized alloys

| Alloy | $R_s$ | $CPE_{dl}$ | | $R_{ct}$ | $CPE_f$ | | $R_f$ | $L$ | $R_L$ |
|---|---|---|---|---|---|---|---|---|---|
| | Ω·cm$^2$ | $Y_1$/μΩ$^{-1}$·cm$^{-2}$ | $n_1$ | Ω·cm$^2$ | $Y_2$/μΩ$^{-1}$·cm$^{-2}$ | $n_2$ | Ω·cm$^2$ | H·cm$^2$ | Ω·cm$^2$ |
| B1 | 1.843 | 91.22 | 0.46 | 31.12 | 221.8 | 0.93 | 6.17 | 133.8 | 50.37 |
| BA11 | 4.912 | 61.36 | 0.72 | 107.5 | 20.02 | 0.99 | 3.77 | 71.9 | 52.82 |
| BZ11 | 5.52 | 41.15 | 0.79 | 139.7 | 17.79 | 0.99 | 6.42 | 277.2 | 52.77 |
| BC11 | 4.165 | 49.78 | 0.88 | 32.3 | 134.7 | 0.94 | 6.16 | 807.9 | 72.29 |

ating at intermediate frequencies. Furthermore, $L$ and $R_L$, respectively, denote inductance and inductive impedance of the solution.[20]

The Bode diagrams of homogeneous alloys in **Figure 7a** illustrate that a higher low-frequency impedance modulus corresponds to a greater mass conversion resistance.[21] As shown in **Figure 7b**, the Nyquist plots for the four alloys consist of a small capacitance loop and a large capacitance loop in both the high and mid-frequency regions, as well as a low-frequency inductive reactance arc, which can be verified by the presence of a time constant in the corresponding Bode phase angle plot, as shown in **Figure 7c**. According to the peak value of the phase-angle-frequency curve in **Figure 7c**, it can be determined that there are two peaks in all four alloys, indicating that the electrochemical impedance spectrum has two time parameters. These parameters are represented by a small semicircle corresponding to the high frequency region and a large semicircle corresponding to the low frequency region on the Nyquist curve (as shown in **Figure 7b**). In the high-frequency region, the capacitor circuit illustrates the charge transfer, while in the medium-frequency region it represents the product film formation. The relaxation of the corrosion product film leads to the formation of a low-frequency inductive loop on the surface of the $\alpha$-Mg matrix.[22] The corrosion resistance of BC11 alloy decreases as the diameter of its capacitor ring decreases.[23,24] In contrast, BZ11 alloy exhibits the largest capacitance loop diameter and impedance modulus Zmod (**Figure 7b**), indicating superior corrosion resistance compared to other alloys.

The equivalent circuit diagram of the alloy is depicted in **Figure 7d**. The diameter of the high-frequency bulk reactance arc represents the charge transfer resistance ($R_{ct}$) between the electrode and the corrosive medium.[25] A larger $R_{ct}$ indicates a more challenging charge transfer for the alloy. Upon fitting, it was observed that BZ11 alloy exhibits the highest $R_{ct}$, suggesting superior corrosion resistance, which aligns with the experimental findings on hydrogen evolution.

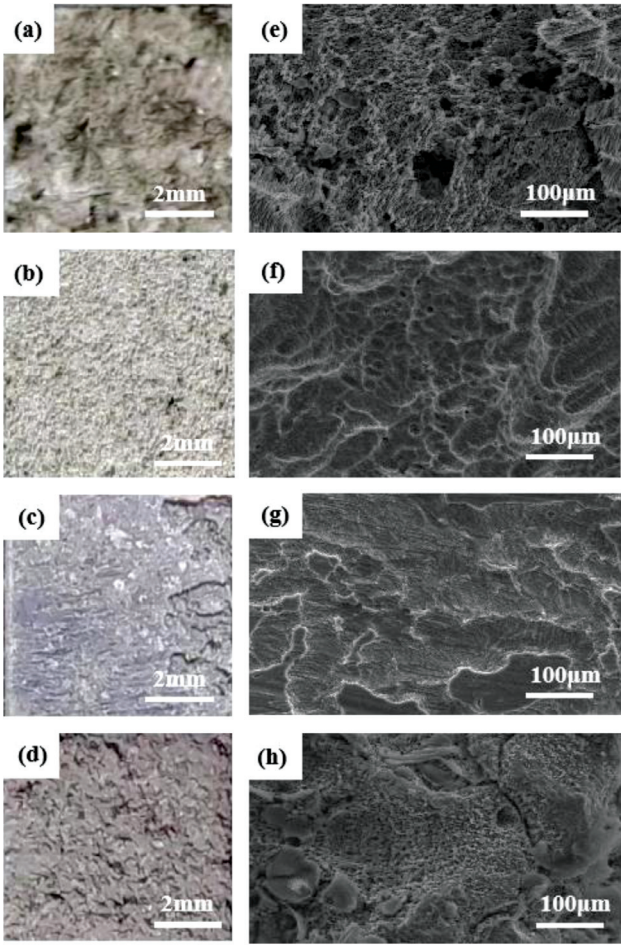


**Figure 8:** Corrosion morphologies of homogeneous B1 (a, e); BA11 (b, f); BZ11 (c, g) and BC11 (d, h) alloys

### *3.4 Corrosion morphologies*

Macroscopic corrosion morphologies and SEM images of homogeneous B1, BA11, BZ11, and BC11 alloys immersed in a 3.5 *w*/% NaCl solution for 24 h are depicted in **Figure 8**. Corrosion pits that form after spalling of the alloy's corrosion products, distributed across the entire surfaces of all four types of alloys are clearly visible. The B1, BA11, and BC11 alloys exhibit a loss of metallic luster on their surfaces, with numerous pits of varying depths observed in B1 alloy (**Figure 8a**). In comparison to B1 alloy, the surface corrosion of BA11 alloy is shallower, with only a very small portion remaining uncorroded (**Figures 8c and 8g**). This suggests that the addition of aluminum can enhance the corrosion resistance of the alloy to some extent. The corrosion morphology of BZ11 alloy is depicted in **Figure 8c**, revealing partial retention of the metallic luster in its macroscopic appearance. Microscopically, the local morphology of BZ11 alloy (**Figure 8d**) demonstrates a reduced corrosion area compared to that of BA11 alloy, with distinct smooth regions remaining uncorroded. These findings indicate that the addition of Zn can effectively inhibit corrosion to some extent. However, BC11 alloy exhibits more severe surface pitting and corrosion cracks (**Figure 8d and 8h**), indicating a pronounced progression of the alloy degradation. This observation aligns with the results obtained with electrochemical experiments and hydrogen evolution experiments.

The corrosion morphologies of homogeneous B1, BA11, BZ11, and BC11 alloys with corrosion products after immersion in a 3.5 *w*/% NaCl solution for 24 h is depicted in **Figure 9**. Apart from BZ11 alloy, the surfaces of B1, BA11, and BC11 alloys exhibit corrosion cracks. Comparatively speaking, B1 alloy (**Figure 9a**) displays wider corrosion cracks than BA11 and BC11 alloys. Meanwhile, BA11 alloy exhibits smaller corrosion cracks (**Figure 9b**). In contrast, pitting corrosion is observed on the surface of BZ11 alloy (**Figure 9c**), with

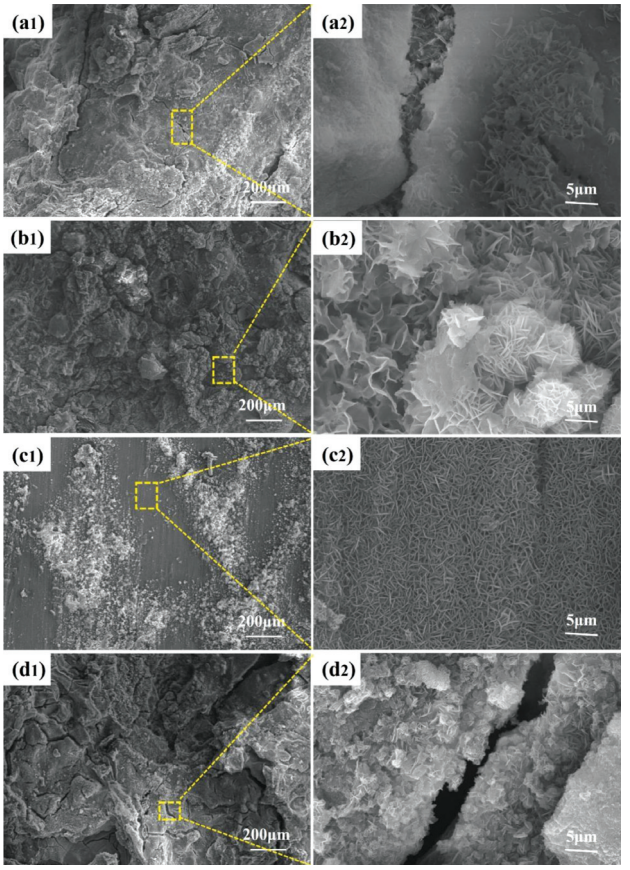


**Figure 9:** Corrosion morphologies of homogeneous B1 (a1, a2); BA11 (b1, b2); BZ11 (c1, c2) and BC11 (d1, d2) alloy films carrying corrosion products

some areas remaining uncorroded or flat. On the other hand, dense spherical corrosion products extensively cover BC11 alloy's surface (**Figure 9d**).

## 4 DISCUSSION

Grain size and second phase are two major factors influencing the corrosion rate of magnesium alloys. Except for BC11 alloy, the remaining three alloys have smaller fractions of second phase (**Figure 1**). **Figure 3** illustrates the influence of alloying elements on the grain size. The additions of 1 *w*/% of Al, Zn, and Cu refine the grain structure to varying degrees. Corrosion mechanism diagrams for the homogeneous B1, BA11, BZ11, and BC11 alloys are depicted in **Figure 9**.

After 24 h of corrosion, surface corrosion cracks were observed on the Mg-1Bi alloy (**Figure 8**), indicating compromised integrity of the corrosion product film and diminished corrosion resistance. The emergence of these cracks can be attributed to the reduction reaction occurring at the anode during the corrosion process, generating the $H_2$ gas that continuously escapes upwards, thereby damaging the protective surface layer and leading to crack formation. The presence of a greater number of cracks corresponds to a higher concentration of $H_2$ and consequently exacerbates damage to the oxide layer, ultimately resulting in increased corrosion.

The addition of 1 *w*/% Al refines the alloy grain by 31 % so that the grain size shrinks from 1≈2 mm to 0≈1.2 mm. The addition of Al increases the area fraction of the second phase of the alloy, and a large number of second phases limits the grain growth. The higher the growth limiting factor (the *GRF* or *Q* value) for the second element in the alloy, the stronger is the inhibition effect on the grain growth and the more obvious is the refinement effect. Studies have shown that the *Q* value of Al is 4.32,[26] indicating that the addition of Al can have a grain-refining effect. The results show that the grain refinement is more obvious when the Al content is higher than 2.0 *w*/%. When the Al content is below 1.0 *w*/%, its influence on the grain structure is small.[27,28] Compared with B1 alloy, the addition of Al increases the average size and area fraction of the precipitated phase (**Table 2**). However, the results of the hydrogen-evolution weight-loss experiment and electrochemical experiment show that its corrosion resistance is better than that of B1 alloy, indicating that the galvanic corrosion of the second phase and the matrix cannot be the most important factor affecting the corrosion of the alloy. After 24 h corrosion of BA11 alloy in the 3.5 *w*/% NaCl solution, a corrosion product film was formed on the surface (**Figure 8b**), which provided local protection. Due to the continuous precipitation of hydrogen, relatively loose corrosion products were locally destroyed, and some fine corrosion cracks were formed (**Figure 8b**), resulting in a relatively sparse corrosion product film. The BA11 surface product film is denser than that of B1 alloy, and can slow down the rate of corrosion.

Zn has a high solubility, and up to 1.6 *w*/% of Zn can be completely dissolved in an $\alpha$-Mg matrix at room temperature.[29] Therefore, when the amount of Zn is below the solubility limit, the alloying element Zn tends to be incorporated into the $\alpha$-Mg matrix. Thus, Zn dissolves in the $\alpha$-Mg matrix as a solute without forming a new second phase (**Figure 1**). The results show that Zn atoms exist in $\alpha$-Mg as solute atoms, while the solid solution tends to be in a lower energy state, and the formation of Mg-Zn clusters is relatively stable. Therefore, after the addition of Zn, Mg atoms are more easily combined with Zn atoms.[30] The alloy is in a more stable state, which also plays a positive role in its corrosion resistance. Moreover, the Q value of Zn is 5.008,[26] and the addition of Zn refines the grain size of the alloy by 60 %. If the film of the corrosion product is dense, the grain boundary can be used as a corrosion barrier to prevent corrosion expansion. Generally, the solute concentration at the grain boundary is higher than that inside the grain, and the grain boundary region, acting as the cathode, accelerates corrosion in the central region of the grain. The decrease in the grain size leads to an increase in grain boundaries and a decrease in the average solute concentration in the grain boundary region, which is equivalent

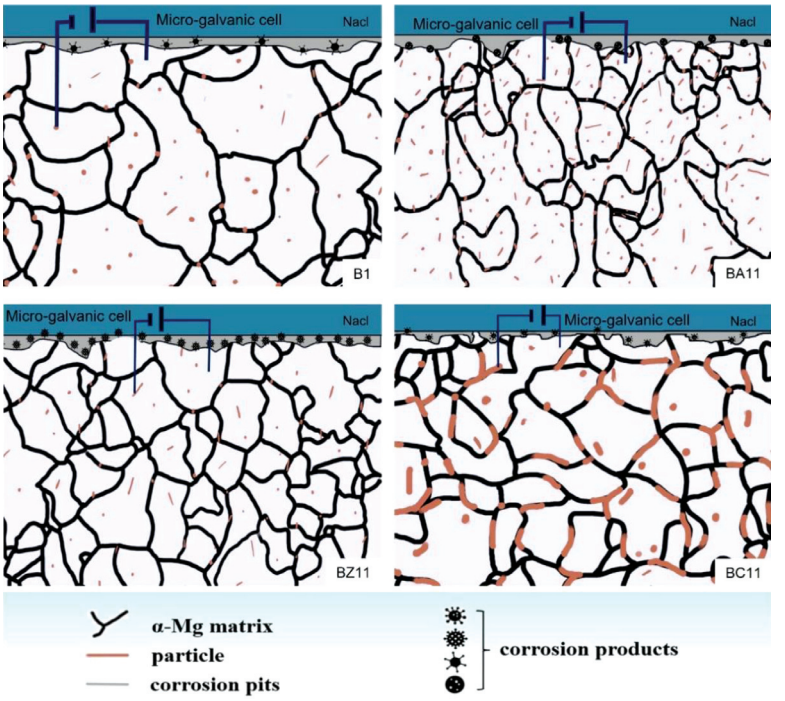


**Figure 10:** Corrosion mechanisms of homogenized B1, BA11, BZ11 and BC11 alloys

to increasing the solute concentration in the alloy matrix, thus increasing the self-corrosion potential of the alloy matrix.[31,32]

After the addition of 1 *w*/% Cu, in addition to the $\alpha$-Mg phase and $Mg_3Bi_2$ phase, there is also a new $Mg_2Cu$ phase. The area fraction and average size of the second phase increase significantly (**Table 3**). According to the research, the Q value of Cu is 5.28, which can play a role in refining grains.[26] In addition, the dispersed particles of the second phase mainly gather at the grain boundaries. The grain size is refined by 43 %, which is slightly higher than that of BA11 alloy. Due to the increase in the grain boundaries, a large number of second phases exist at the grain boundaries and they are connected into a network structure. Due to a potential difference in the corrosion process, there is obvious micro-galvanic corrosion between the intermetallic phase and the $\alpha$-Mg matrix. Pitting preferentially occurs between the matrix and the second phase.[33] In a corrosion process, $Mg_3Bi_2$ and $Mg_2Cu$ particles act as the cathode sites for $H_2$ precipitation, resulting in a decrease in the density of the corrosion product layer. With the progress of corrosion, the second phase particles may fall off, leaving corrosion pits on the surface. The corrosion pits formed due to particles falling off increase the surface roughness of the alloy, leading to an increase of the contact area between the magnesium alloy and the solution, thus increasing the hydrogen precipitation rate. According to the results of the hydrogen-evolution weight-loss experiment, the formation rate of the corrosion product film of BC11 alloy may be greater than the rate of hydrogen precipitation before the 4$^{th}$ hour, so the corrosion rate of B1 alloy is higher than that of BC11 alloy. However, after the 4$^{th}$ hour, the corrosion rate may increase rapidly, and the corrosion resistance may decrease due to the second phase shedding in BC11 alloy.

## 5 CONCLUSION

The influences of the microstructure and corrosion behavior on four types of homogeneous magnesium alloys, namely B1, BA11, BZ11, and BC11, were investigated. The findings are as follows:

1) Electrochemical experiments revealed that all four alloys exhibited similar electrochemical impedance spectroscopy (EIS) diagrams consisting of a high-frequency capacitive loop, a medium-frequency capacitive loop, and a low-frequency inductive loop. Among them, BZ11 alloy demonstrated superior corrosion resistance with a corrosion rate of 0.548 mm·y-1 due to its fine grain size and limited amount of dispersed second-phase particles. Hydrogen evolution experiments indicated that the hydrogen evolution rate for B1, BA11, and BZ11 alloys increased linearly with the corrosion time; among them, BZ11 alloy displayed the highest level of corrosion resistance.

2) Scanning electron microscopy (SEM) combined with energy-dispersive X-ray spectroscopy (EDS) were employed for microscopic characterization of the four magnesium alloys. The results revealed localized corrosion in all four alloys; galvanic corrosion between the second-phase particles and the matrix was particularly noteworthy and identified as the primary cause for BC11 alloy's corrosive behavior. The additions of 1 *w*/% Al,

Zn, Cu led to significant reductions in the grain size by 31 %, 60 %, and 43 %, respectively. The X-ray diffraction (XRD) analysis revealed $\alpha$-Mg phase, along with block-like or strip-like $Mg_3Bi_2$ phases as secondary phases in Mg-Bi alloy. Mg-Bi-1Al and Mg-Bi-1Zn still contained $\alpha$-Mg phase, along with $Mg_3Bi_2$ phase, while Mg-Bi-1Cu mainly consisted of $\alpha$-Mg, $Mg_3Bi_2$, and reticular $Mg_2Cu$ phases.

## Acknowledgements

The authors acknowledge the Natural Science Foundation of Fujian Province [2021J05232] and Science and Technology Planning Project of Longyan [2021LYF9012].

## 6 REFERENCE

[1] R. Decker, The renaissance in magnesium, Advanced Materilas & Processes, 154 (**1998**), 3133

[2] J. R. Thomas, L. A. Darry, High ductility magnesium alloys in automotive applications, Advanced Materials & Processes, 145(**1994**), 28–32

[3] Q. A. Li, Q. Zhang, C. Li, et al., Effects of Bi on Mechanical Properties of Magnesium Alloy AZ81, Advanced Materials Research, (**2011**), 284–286, 1693–1696

[4] W. Xu, W. Cheng, Z. Guo, et al., Development of dilute Mg–Bi alloy sheet with good synergy of corrosion-resistance and tensile properties, Journal of Materials Research and Technology, 25 (**2023**), 3929–3942

[5] P. Predko, D. Rajnovic, M. L. Grilli, et al., Promising methods for corrosion protection of magnesium alloys in the case of Mg-Al, Mg-Mn-Ce and Mg-Zn-Zr: A recent progress review, Metals, 11 (**2021**), 1133

[6] J. E. Lein, T. K. Aune, K. Nisancioglu, The role of magnesium aluminium (Mg17Al12) phase in the corrosion of magnesium alloy AZ91, Corrosion, Houston TX, 45 (**1989**), 741–748

[7] D. S. Yin, E. L. Zhang, S. Y. Zeng, Effect of Zn on mechanical property and corrosion property of extruded Mg-Zn-Mn alloy, Transactions of Nonferrous Metals Society of China, 18 (**2008**), 763–768

[8] R. Zeng, Review of studies on corrosion of magnesiumalloys, Transactions of Nonferrous Metals Society of China, 16 (**2006**), 763–771

[9] M. Zhang, F. Li, Z. Guo, et al., Effect of a bimodal grain structure on corrosion behavior and tensile properties of low-alloyed Mg–1Bi–1Zn–1Ag alloy, Journal of Materials Research and Technology, 24 (**2023**), 9249–9260

[10] Y. Xudong, W. Peng, C. Lanyue, et al., Microstructural effects on mechanical properties and degradation behavior of Mg-Cu alloy, Materialia, 16 (**2021**)

[11] P. Jiang, C. Blawert, J. Bohlen, et al., Corrosion performance, corrosion fatigue behavior and mechanical integrity of an extruded Mg-4Zn-0.2Sn alloy, Journal of Materials Science & Technology, 59 (**2020**), 107–116

[12] C. Xiang, Z. Xiao, H. Ding, et al., Compressive properties and energy absorption characteristics of extruded Mg-Al-Ca-Mn alloy at various high strain rates, Materials, 14 (**2020**), 87

[13] W. N. Tang, S. S. Park, B. S. You, Effect of the Zn content on the microstructure and mechanical properties of indirect-extruded Mg–5Sn–xZn alloys, Materials & Design, 32 (**2011**), 3537–3543

[14] C. Wang, S. Guo, L. Zeng, et al., Effects of second phases on microstructure, microhardness, and corrosion behavior of Mg-3Sn-(1Ca) alloys, Materials, 12 (**2019**), 2515–2527

[15] W. Xu, W. Cheng, Z. Guo, et al., Development of dilute Mg–Bi alloy sheet with good synergy of corrosion-resistance and tensile properties, Journal of Materials Research and Technology, 25 (**2023**), 3929–3942

[16] W. Cheng, S. Ma, Y. Bai, et al., Corrosion behavior of Mg-6Bi-2Sn alloy in the simulated body fluid solution: the influence of microstructural characteristics, J. Alloys Compd, 731 (**2018**), 945–954

[17] Z. Zhang, H. Hou, Y. Zhang, et al., Effect of calcium addition on the microstructure, mechanical properties, and corrosion behavior of AZ61-Nd alloy, Advanced Composites and Hybrid Materials, 6 (**2023**), 50

[18] Y. Liu, J. Wen, H. Li, et al., Effects of extrusion parameters on the microstructure, corrosion resistance, and mechanical properties of biodegradable Mg–Zn–Gd–Y–Zr alloy, J. Alloys Compd., 891 (**2022**)

[19] T. Y. Pan, L. B. Wang, Finite-element analysis of chemical transport and reinforcement corrosion induced cracking in variably saturated heterogeneous concrete, Journal of Engineering Mechanics-asce, 137 (**2011**), 334–345

[20] Z. Yang, A. Ma, B. Xu, et al., Corrosion behavior of AZ91 Mg alloy with a heterogeneous structure produced by ECAP, Corrosion Science, 187 (**2021**), 109517

[21] H. Wu, S. Xiao, D. Chen, et al., Effects of diamond like carbon film on the corrosion behavior of NdFeB permanent magnet, Surface and Coatings Technology, 312 (**2017**), 66–74

[22] S. Yin, W. Duan, W. Liu, et al., Improving the corrosion resistance of MgZn1. 2GdxZr0. 18 (x= 0, 0.8, 1.4, 2.0) alloys via Gd additions, Corrosion Science, 177 (**2020**), 108962

[23] J. Liu, J. Zhang, J. Tang, et al., Polydimethylsiloxane resin nanocomposite coating with alternating multilayer structure for corrosion protection performance, ES Materials & Manufacturing, 10 (**2020**), 29–38

[24] S. Mishra, P. Chaudhary, B. C. Yadav, et al., Fabrication and characterization of an ultrasensitive humidity sensor based on chalcogenide glassy alloy thin films, Engineered Science, 15 (**2021**), 138–147

[25] H. R. Bakhsheshi-Rad, E. Hamzah, H. Y. Tok, et al., Microstructure, In Vitro Corrosion Behavior and Cytotoxicity of Biodegradable Mg-Ca-Zn and Mg-Ca-Zn-Bi Alloys, Journal of Materials Engineering & Performance, 26 (**2017**), 653–666, DOI:10.1007/s11665-016-2499-0

[26] E. Karakulak, A review: Past, present and future of grain refining of magnesium castings, Journal of Magnesium and Alloys, 7 (**2019**), 355–369

[27] P. Hoyer, G. L. Angrisani, C. Klose, et al., Influence of aluminium on the corrosion behaviour of binary magnesium–aluminium alloys in saline solutions, Materials and Corrosion, 65 (**2014**), 23–30

[28] Y. Cheng, T. W. Qin, H. M. Wang, et al., Comparison of corrosion behaviors of AZ31, AZ91, AM60 and ZK60 magnesium alloys, Transactions of Nonferrous Metals Society of China, 19 (**2009**), 517–524

[29] T. B. Massalski, Binary Alloy Phase Diagrams, American Society for Metals, Ohio, 1986

[30] J. Zhao, B. Luo, K. He, et al., Effects of minor Zn content on microstructure and corrosion properties of Al-Mg alloy, Journal of Central South University, 23 (**2016**), 3051–3059

[31] M. Alvarez-Lopez, M. D. Pereda, J. A. del Valle, M. Fernandez-Lorenzo, et al., Corrosion behaviour of AZ31 magnesium alloy with different grain sizes in simulated biological fluids, Acta Biomater., 6 (**2010**), 1763–1771

[32] P. Metalnikov, G. Ben-Hamu, Y. Templeman, K. S. Shin, et al., The relation between Mn additions, microstructure and corrosion behavior of new wrought Mg-5Al alloys, Mater. Charact., 145 (**2018**), 101–115

[33] S. M. Baek, J. S. Kang, J. C. Kim, et al., Improved corrosion resistance of Mg-8Sn-1Zn-1Al alloy subjected to low-temperature indirect extrusion, Corros. Sci., 141 (**2018**), 203–210